RESEARCH ARTICLE | OCTOBER 08 2024

The effect of non-perpendicular incidence angles on discharge characteristics in an argon atmospheric plasma jet impinging on metal, water and glass substrates



Phys. Plasmas 31, 103507 (2024) https://doi.org/10.1063/5.0214063





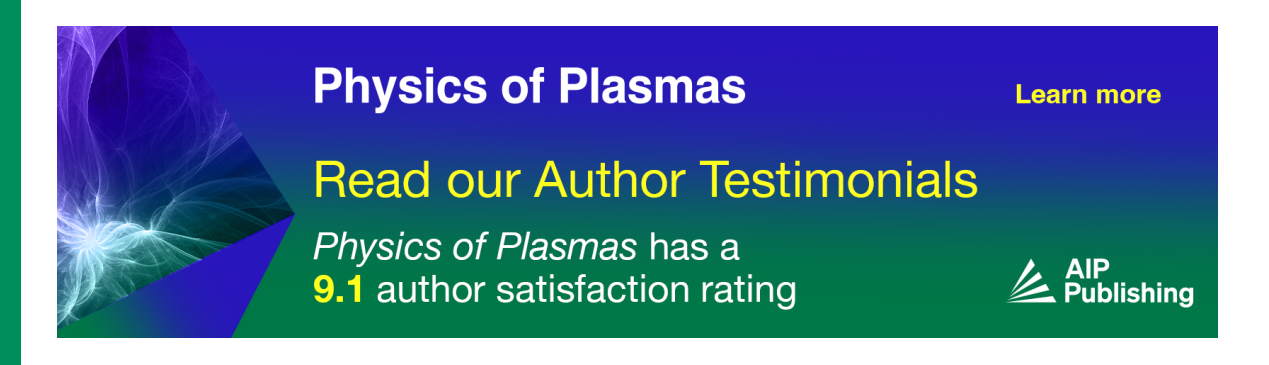
Articles You May Be Interested In

Effective ionization coefficient in mixtures of Ar and O_2 determined using the Townsend discharge AIP Advances (October 2022)

Dielectric exposed on DC-pulsed helium plasma jet: Hollow distribution of the surface electric field Phys. Plasmas (November 2023)

Construction and characterization of AC atmospheric pressure plasma jet of argon gas

AIP Conference Proceedings (December 2022)





The effect of non-perpendicular incidence angles on discharge characteristics in an argon atmospheric plasma jet impinging on metal, water and glass substrates

Cite as: Phys. Plasmas 31, 103507 (2024); doi: 10.1063/5.0214063 Submitted: 15 April 2024 · Accepted: 9 September 2024 · Published Online: 8 October 2024







Jiayin Li 🕞 and Minkwan Kim^{a)} 🕞



AFFILIATIONS

School of Engineering, University of Southampton, Southampton SO17 1BJ, United Kingdom

^{a)}Author to whom correspondence should be addressed: m.k.kim@soton.ac.uk

ABSTRACT

The spatial-temporal discharge behavior of an AC argon plasma jet tilted at non-perpendicular incidence angles (60°, 45°, and 30°) interacting with an ungrounded metal, water, and glass plate placed on the jet propagation track was studied by the fast-imaging technique. The conductivity of surface and incidence angles plays an essential role in the discharge current and dynamic process of the plasma jet. The nearly consistent time delay between subsequent breakdowns occurred four times for metal and two times for glass treatments. The mean luminous intensity of the plasma in one discharge cycle at the discharge area between ground electrode and target surface region for the water and glass case decreased by 39.5% and 20.5% when the incidence angle decreased from 60° to 30°, respectively. In particular, the incidence angle and gas flow rate notably impacted the spatial extension behavior created on the glass surface but had no significant difference in discharge characteristic of plasma jet with metal case. In addition, two equivalent circuit models were developed based on the simulation of the microdischarges and the geometry of the "plasma jet-substrate" system, respectively. These results will obtain further insight into the underlying mechanisms of plasma-target interaction and facilitate the designing of appropriate jet for environmental and biomedical applications.

© 2024 Author(s). All article content, except where otherwise noted, is licensed under a Creative Commons Attribution-NonCommercial 4.0 International (CC BY-NC) license (https://creativecommons.org/licenses/by-nc/4.0/). https://doi.org/10.1063/5.0214063

I. INTRODUCTION

Atmospheric pressure plasma jets (APPJs) have drawn considerable attention mainly due to their promising application for materials processing,¹⁻⁴ biomedicine,⁵⁻⁷ and water treatment.⁸⁻¹¹ APPJs have the remarkable capability to produce chemically rich plasma plumes in the open air, which facilitates ions, electrons, photons, and reactive species transporting to the target, thus enabling the treatment of extensive and irregular surfaces. 12,13 Indeed, the target can be influenced by the electrical properties of the plasma, and vice versa it also impacts the discharge characteristics in various ways. These intricate effects constitute the plasma-target interaction intertwined with the electrical properties of the target.14

In general, surfaces of targets typically adopt a perpendicular orientation to the axis of the jet tube. Upon contact with the target surface, the parameters of plasma jets could undergo a significant perturbation. However, positioning the target at an angle relative to the tube axis induces substantial alterations in both gas flow regime and plasma parameters. Indeed, the incidence angle could boost the treatment surface area covered by the plasma or boost the activity of the plasma activated water.¹⁷ So far, several studies investigated the interaction of APPJs with a tilted target. Nishime et al. 18 utilized a tilted plasma jet for polyethylene terephthalate polymer treatment to increase the modified area by decreasing the angle between the jet and substrate, thus allowing more ROS (reactive oxygen species) covered over the substrate in a wilder area. Damany et al. 19 investigated the dynamics process of an argon plasma jet when interacting with an ungrounded glass plate. They found that the ionization waves (IWs) initially propagate following the trajectory of the tube axis, then deviate toward the glass surface and finally expand on the plate. Hosseinpour et al.²⁰ studied the impact of incidence angle and gas flow rate of an argon jet on the morphology of silver thin films, and an incidence angle of 60° remarkably enhanced the grain uniformity and also modified the grains' shape. Slikboer et al.²¹ and Razavizadeh et al.²² reported that the APPJs at 45° incidences charging on Bi₁₂SiO₂₀ crystal surface

and the gas flow rate are the main factor on the electric field distribution shape of the target surface discharge. The recent study by, Liu *et al.*²³ on the split and deviation of incident waves (IWs) demonstrates that the tilt angle and relative permittivity of a target can influence the position of the IW interaction with the target by altering the surface ionization wave (SIW).

Previous studies usually explore the effect of some of these parameters, such as plume incidence angle, 20,24,25 gas flow rate, 26 and conductivity of the target ^{27,28} on the plasma-target interaction process. However, few studies, if any, consider the effect of the abovementioned parameters altogether. Moreover, several equivalent electrical models have been proposed to characterize the discharge behaviors of plasma-target systems, in which the DBD plasma is represented by either a temporally variable resistance^{29,30} or a voltage-controlled current source (VCCS) combined with a temporally variable resistance.³¹ It should be noted that the discharge behaviors of the APPJ interacting on the substrates are not fully align with DBD, which only generated plasma between the electrode regimes. A model to characterize the whole discharge behavior from DBD stage to the jet-target interaction stage should be developed. Therefore, systematic and comprehensive investigations of the discharge characteristics in tilted APPJs impinging on the different substrates need to be performed. For the optimization of plasma jet applications, it is important to precisely manipulate over these setup parameters that enable customizing the reactivity of the plasma and its interaction with the target surface.

In this work, a tilted AC driven argon jet propagates in surrounding air and encounters ungrounded targets including a conductive substrate (metal piece), a high-resistance conductor (de-ionized water), and a dielectric substrate (glass plate). The effect of non-perpendicular incidence angles (60°, 45°, and 30°) on the spatial–temporal discharge behavior of the plasma is described using a fast-imaging technique. The results will obtain further insight into the underlying mechanisms of plasma-target interaction and serve as a useful reference to inform environmental and biomedical applications.

II. EXPERIMENTAL SETUP

The schematic setup of the plasma jet device used in this work is shown in Fig. 1(a). A high-voltage (H.V.) electrode made of a stainless steel needle was inserted into a 10-cm-long quartz tube. The inner and

outer diameter of the nozzle is 4 and 6 mm, respectively. The radius of the curvature at the electrode tip is almost 1.5 mm. A ring electrode made of copper tape with a width of 1 mm and thickness of 100 μ m was wrapped outside the quartz tube and used as a grounded electrode, which was 2 mm away from the nozzle end. The distance between the tip of the needle and the ground electrode is about 3 mm. Argon (99.999%) is used as a working gas with gas flow rate at 2 or 1 L/min. The gas flow velocity at the plasma source is estimated as 1.3 and 2.6 m/ s to achieve laminar conditions.³³ Three kinds of target substrates were treated with different plasma jet incidence angles of 60° , 45° , and 30° (with respect to the x-axis): (1) a piece of metal plate made of stainless steel with thickness of 2 mm; (2) deionized water with depth of 2 mm, electrical conductivity of 2×10^{-4} sm⁻¹ and permittivity of 90; and (3) a piece of dry, flat glass plate also with thickness of 2 mm, electrical conductivity of 10^{-13} sm⁻¹ and relative permittivity of 4.7. The distance D between the tip of the needle and the surface of substrates was fixed at 15 mm. A schematic drawing of the treatment is presented in Fig. 1(b). For convenience, the plasma plume with an incidence angle of 60°, 45°, and 30° operation will further be referred to as the 60-degree, 45-degree, and 30-degree substrate treatment, respectively.

The plasma jet was powered by an AC high-voltage source (V_{p-p} : 0–20 kV), created from a sinusoidal waveform signal by a signal generator (AFG1062, Tektronix) and an audio power amplifier (CDi DriveCore 2|600, Crown). The frequency and the peak-to-peak value of sinusoidal high voltage were fixed at 5 kHz and 6.0 kV, respectively. The electrical characteristics of the plasma jet were recorded by an oscilloscope (MDO34, Tektronix) and detected by a high-voltage probe (P6015A, Tektronix) for the applied voltage and a Rogowski coil (Model 6585, Pearson Electronics) for the current, respectively. The plasma images were recorded with a digital single-lens reflex camera (Nikon D5600, AS-F Micro NIKKOR 40 mm). The dynamic images were taken by an ICCD camera (DH334T, Andor. Exposure time: 0.1 s, width: 0.2 μ s, increment: 0.2 μ s).

III. RESULTS AND DISCUSSION

A. Discharge images

Figure 2 shows visible images under incidence angles of 60° , 45° , and 30° interacting with metal, water, and glass plate at an applied

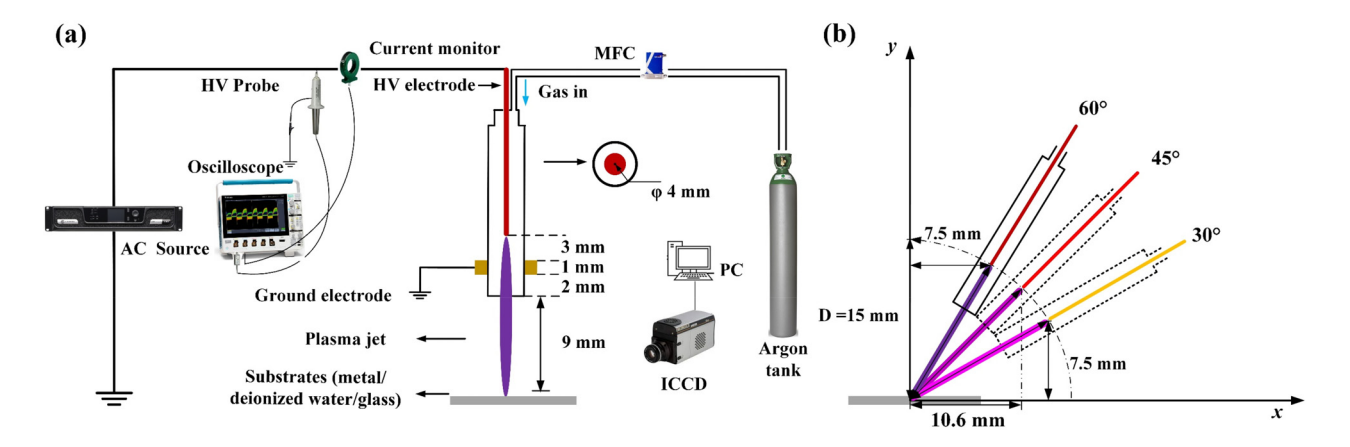


FIG. 1. (a) Schematic setup of the plasma jet and (b) arrangement of the plasma plume with different incidence angles of 60°, 45°, and 30°. The distance between the needle tip and substrate is fixed as D.

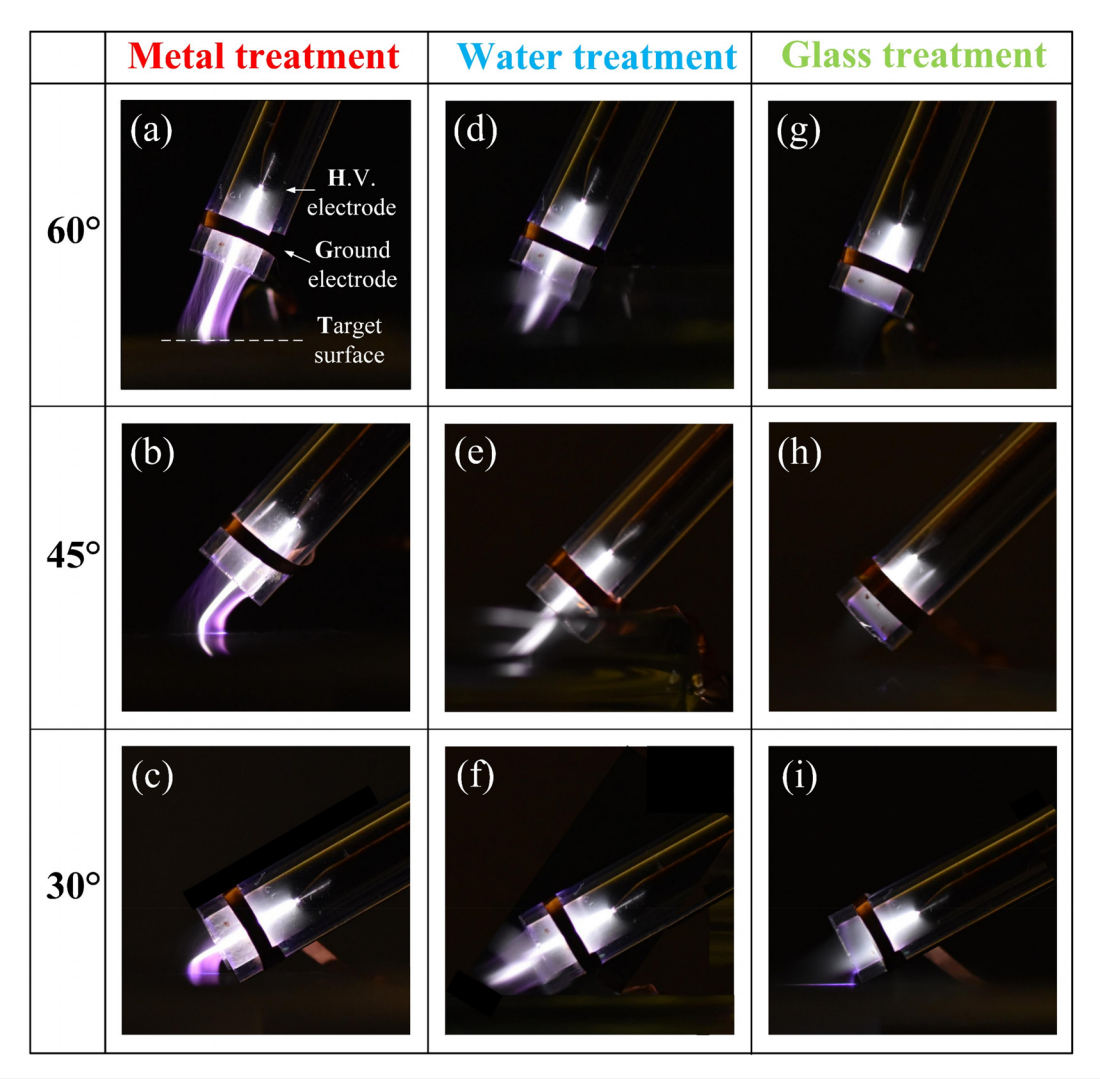


FIG. 2. Discharge images under plasma jet incidence angles of 60° (a)–(c), 45° (d)–(f), and 30° (g)–(i) interacting with metal, water, and glass plate (exposure time 0.2 s, ISO 800 f/4)

voltage of 6 kV. The discharge can be categorized into three distinct regions, as indicated by the dashed lines in Fig. 2, as follows:

- (1) Filament discharge between the high-voltage electrode (H. V. electrode) and the ground electrode (referred to as H-G region);
- (2) Plasma extending from the ground electrode to the target (referred to as G-T region); and
- (3) Plasma jet interacting with the target surface.

In region I, very bright filaments developed from the H. V. electrode to the ground electrode among three kinds of target cases. In region II, similar bright filaments are observed in metallic target case in Figs. 2(a)-2(c) and water target case in Figs. 2(d)-2(f). No obvious reduction in the diameter of the discharge channel in open air was observed due to the short and small diameter jet used in the experiment. However, the plasma jet became diffuse and appeared as an "ellipse" shape in the glass case in Figs. 2(g)-2(i). The diameter of the

discharge between the G-T region in the glass case [Fig. 2(g)] was larger compared to the copper and liquid case [Figs. 2(a) and 2(d)]. In region III, the plasma jet spread over the surface was more concentrated on the copper surface due to the infinite relative permittivity that excludes the electric field.³⁵

B. Electrical characteristic

Figure 3 shows the typical waveforms of voltage and discharge current measured with the APPJ impinging on different substrates. Numbers 1–7 marked within the circle will be further indicated with the start points of dynamic process. According to Fig. 3(a), with the metal substrate case, four discharge pulses are clearly observed in the current waveform: two at the positive period and other two at the negative period, one of which was a negative directed current. The maximum and the second highest peak values of current (1 and 2) are 34

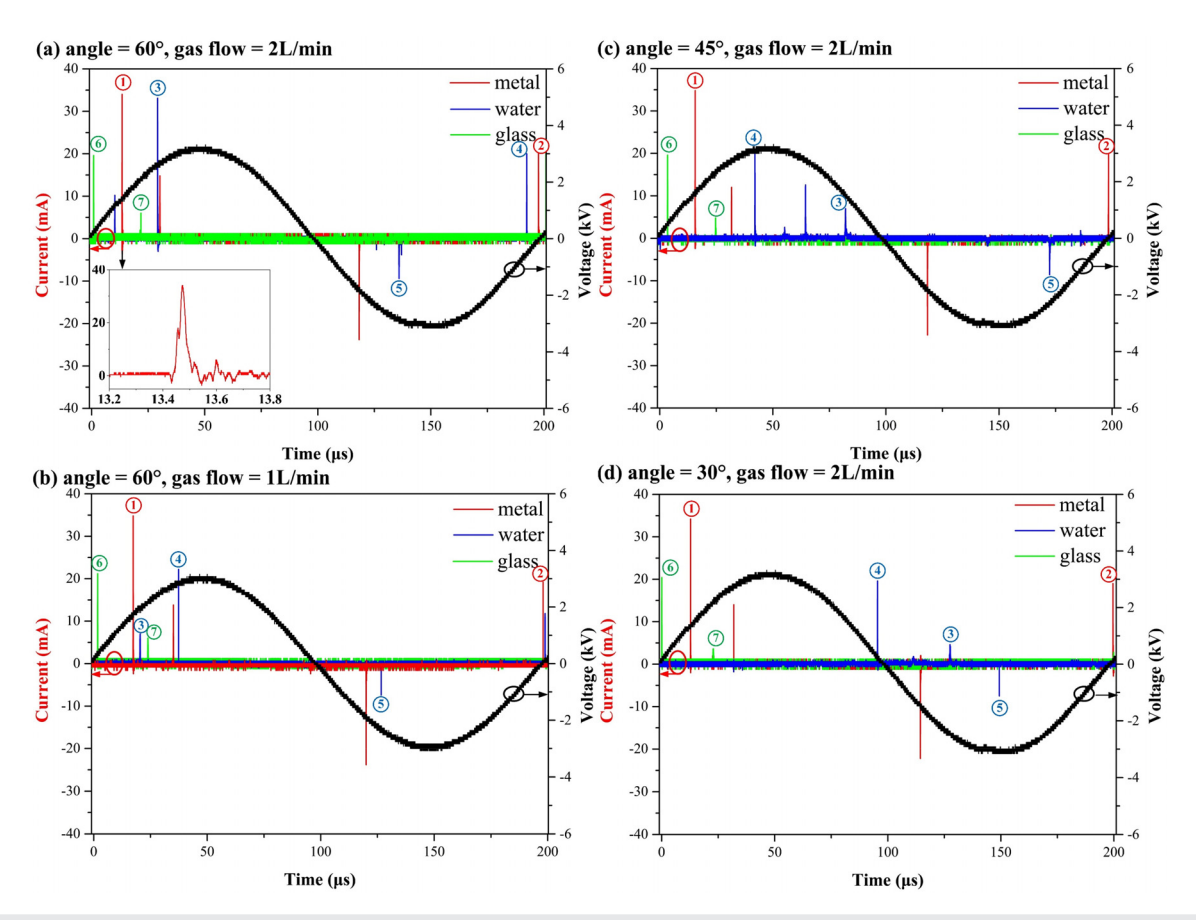


FIG. 3. Discharge current and voltage waveforms. The current waveforms were marked red, blue, and green line corresponding with metal, water, and glass treatment configurations, respectively.

and 20 mA, respectively. To clearly observe the discharge current pulse, it appears in a pulsed discharge mode with a full width at half maximum (FWHM) of approximately 30 ns. For the de-ionized water substrate, the four discharge pulses were similarly observed in one period, but each peak value of current was lower than that of the metal case except for current pulse 4, which is the same value as current pulse 2. The maximum and the minimum peak values of current were current pulse 3 (33 mA) and current pulse 5 (10 mA), respectively. For glass substrates, only two distinct discharge pulses were observed during the positive period (6 and 7), whose peak values were 20 and 6 mA, respectively. When the gas flow rate was reduced from 2 to 1 L/min, the peak current values and discharge times for both metal and glass cases almost remained the same conditions, but the discharge times were not fixed and each peak value of the pulse current decreased for the case of water substrates.

According to Figs. 3(a), 3(c), and 3(d), when the plasma jet incidence angle changed from 60° to 45°, then 30°, two distinct discharge pulses were still observed during the positive period, and discharge time did not change for the glass treatment. The peak value of current No. 6 remained the same, but the peak value of the current No. 7 was decreased. For metal treatment, there was no significant difference in the peak value and position of the pulse current. For water treatment, the discharge times were random and each peak value of pulses current

was reduced. Specially, the number of discharge pulses decreased from four to three times when the plasma plume incidence angle changed from 45° to 30° .

It turned out that the interaction of the APPJ with various substrates reveals specific modes that correlate with the emergence of distinct current pulses. The nearly consistent time delay between subsequent breakdowns can be attributed to the reduction of the volume charge in the channel left by the preceding ionization wave which occurs due to diffusion or volume recombination. Based on the voltage and current waveforms shown in Fig. 3, the input power was estimated to be less than 1 W to avoid the occurrence of arc discharge in our case.

C. Dynamic process

Figures 4–7 illustrate the dynamic process of plasma jet propagation using spatio-temporally resolved ICCD images. The numbers in the scale bar (0–32 000) represent the relative intensity of the color bar, which is proportional to the relative luminous intensity of the plasma. Numbers 1–7 marked with red, blue, and green colors in the circle at the upper-right corner correspond with that of current pulses in Fig. 3 for metal, water, and glass treatment, respectively. The time at the bottom-right corner represents the trigger time of ICCD to start images collection.

1. The effect of gas flow rate

In Fig. 4, the dynamic process images of plasma jet in 60-degree metal, water, and glass treatment at gas flow rate of 2 L/min were taken at different pulse currents. The time-resolved images were captured at the maximum current (current pulse 1) in positive period (started at 14.2 μ s) for the 60-degree metal treatment, which performed the continued light emission in the whole channel at the beginning, then the luminous intensity between the grounded electrode and metal plate gradually decreased but the emission between the high-voltage electrode and grounded electrode still maintained. When dynamic images are taken at the current in the negative period (current pulse 2), the emission is mainly focused on the H-G region area.

For water treatment, only single filament can be observed between the G-T region in series No. 3, and the intensity at the area between the H-G region is higher than that of G-T region. For the position of negative direction in series No. 5, the emission was started from the high-voltage electrode, then propagated to the nozzle end, and finally disappeared. In addition, the emission following the tube axis merely at the area between the H-G region was observed in series No. 4, whose intensity is similar to that in the metal case in series No. 2 and glass case in series No. 6. Specially, the plasma emission taken at the current pulse 7 showed that the streamer initially propagates along the tube axis from the high-voltage electrode to the nozzle end, and subsequently deviated their primary trajectory toward the glass surface.

Then, a surface discharge spatially extended on the glass plate while a plasma was maintained separately within the quartz tube. The plasma jet spreads over a dielectric substrate but does not do that on the metallic substrate case due to the surface dielectric barrier discharge (SDBD) induced by the stray capacitance between a dielectric substrate and ground. Then, the SDBD over glass substrate happens by the formation of the tangential electric field on the surface. Guaitella and Sobota also indicated that the glass surface induced the elongation of the APPJs due to the enhanced electric field at the IW front and the supply of pre-deposited charges on the target surface. In addition, experiments have demonstrated that the discharge in argon is generated in filamentary mode. The propagation of so-called plasma bullets along the DBD plasma jet, which took a much shorter exposure time (nanoseconds), was not observed in our findings due to the difference in exposure time.

Figure 5 shows the dynamic process images of plasma jet in 60-degree metal, water, and glass treatment at gas flow rate of 1 L/min. When the gas flow decreased from 2 to 1 L/min, there was no significant difference in the plasma emission images for the metal treatment in series Nos. 1 and 2, water treatment in series No. 4 and glass treatment in series No. 6. This means the gas flow did not change the discharge between the H-G region, which corresponds with the same peak value of the discharge current. However, the surface discharge in series No. 7 became less than the case of gas flow rate at 1 L/min for the glass treatment case. This phenomenon suggests that the change in

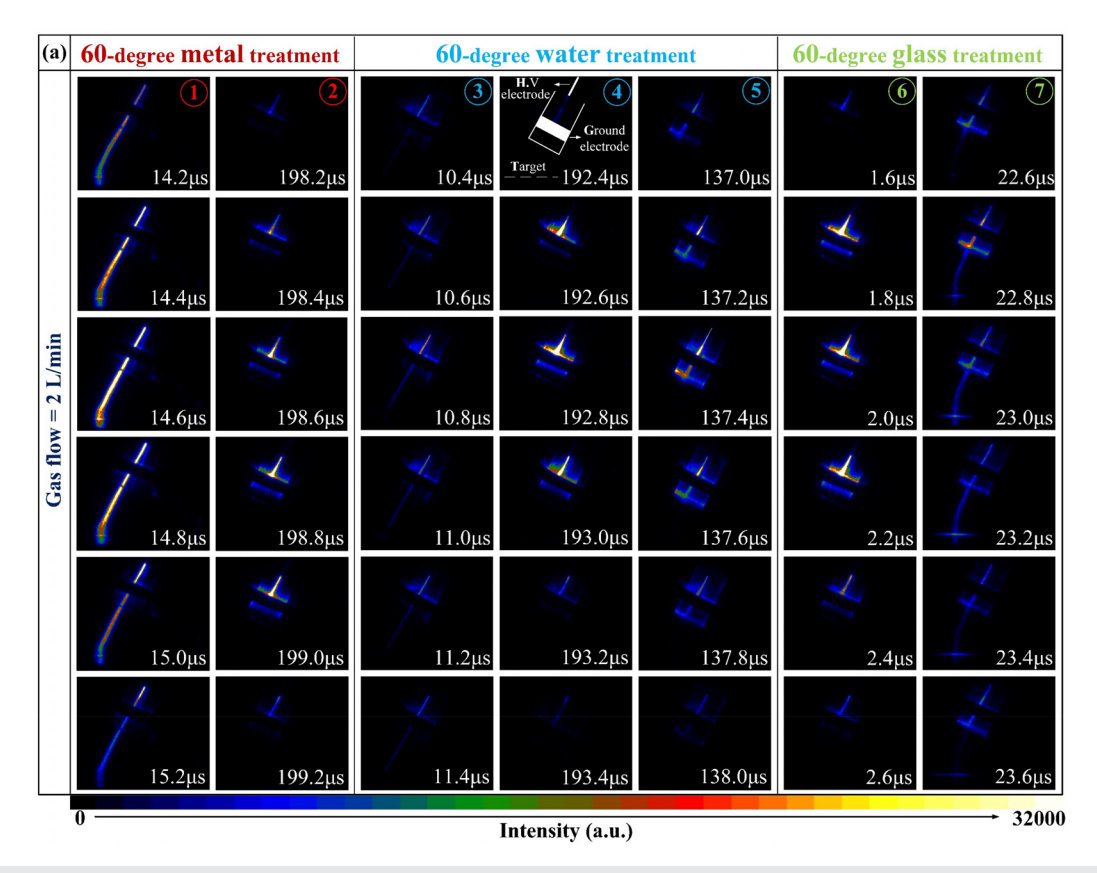


FIG. 4. Time-resolved images of the plasma jet at an incidence angle of 60-degree with metal, water, and glass treatment at gas flow rate of 2 L/min.

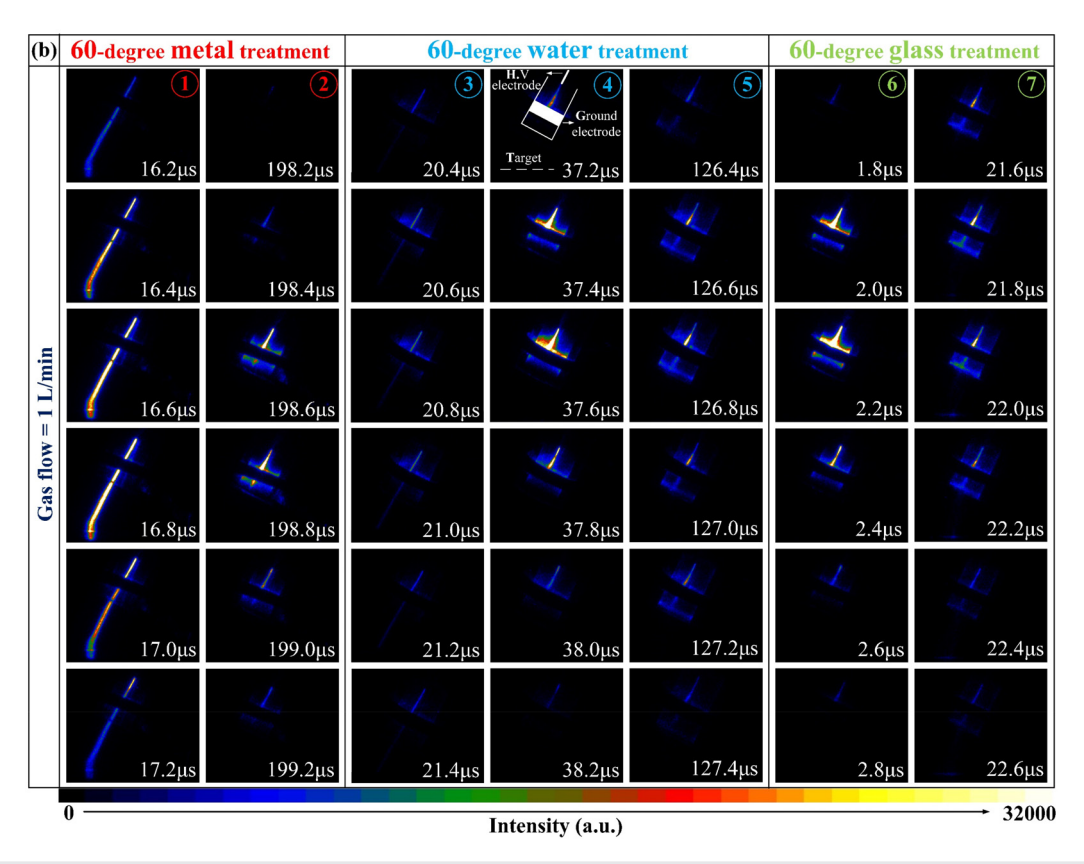


FIG. 5. Time-resolved images of the plasma jet at an incidence angle of 60-degree with metal, water, and glass treatment at gas flow rate of 1 L/min.

gas flow rate can significantly alter the spatial extension of the plasma formed on the glass surface. ¹⁹ For water treatment, the emission density of single filament between the G-T region in series No. 3 and the intensity at the area between the high-voltage electrode and nozzle end were decreased, but the emission density in the area between the H-G region seems not to change in series No. 4.

2. The effect of incidence angles

Figures 6 and 7 show the dynamic process images of plasma jet in 45- and 30-degree metal, water, and glass treatment at gas flow rate of 2 L/min. With regard to the metal treatment, the continuous light emission emerged in the whole channel at the beginning, then the part of emission between the G-T region gradually decreased, and the emission between the high-voltage electrode and grounded electrode was still maintained in series No. 1. This result indicates that the incidence angle of plasma jet and gas flow will not change the discharge behavior of plasma jet impinging on metal plate. As for the discharge area at H-G region, the dynamic process is almost in the same condition as the metal treatment in series No. 2, water treatment in series No. 4, and glass treatment in series No. 6.

For water treatment in Figs. 6 and 7, the discharge would not only propagate from the H-G region but also reach the liquid surface with a single filament in series No. 3. Similarly, the emission propagated from the high-voltage electrode to the nozzle end and finally

disappeared in series No. 5. These discharge behaviors were similar than that of 60-degree treatment case, but the emission density was lower than that case. For glass treatment, the extension of the plasma that develops on the surface gradually disappears when the incidence angle is decreased from 45° to 30°. This is because the incidence angle affects the gas flow distribution and the electric attraction that the target inflicts on the discharge.³²

To quantitatively analyze the behavior of the plasma jet in varying angles and varying conductivities, Fig. 8 shows the mean light intensity in one discharge cycle at various current pulses. No essential differences in emission intensity were observed at the H-G region for metal case at current pulse 2, water case at current pulse 4, and glass case at current pulse 6. This is due to the fixed gap distance at the H-G region. In Fig. 8(a), the maximum luminous intensity was observed in the metal case at H-G region and G-T region, whose values were 3199.82 and 2798.46, respectively. They did not change with the increase in the incidence angles. In Figs. 8(b) and 8(c), the emission intensity of water case at H-G region increases by 17.1% from 762.43 to 892.29, at G-T region increases by 22.8% from 214.32 to 263.54 with increasing incidence angle from 30° to 45°. A similar trend was also observed in the glass case, the emission intensity at H-G region and G-T region was higher than the water case, while the change rate of the emission intensity was lower than that. The emission intensity of glass case at H-G region increases by 5.4% from 1045.79 to 1102.57, at G-T region increases by 13.6% from 518.43 to 588.92 with the increase in

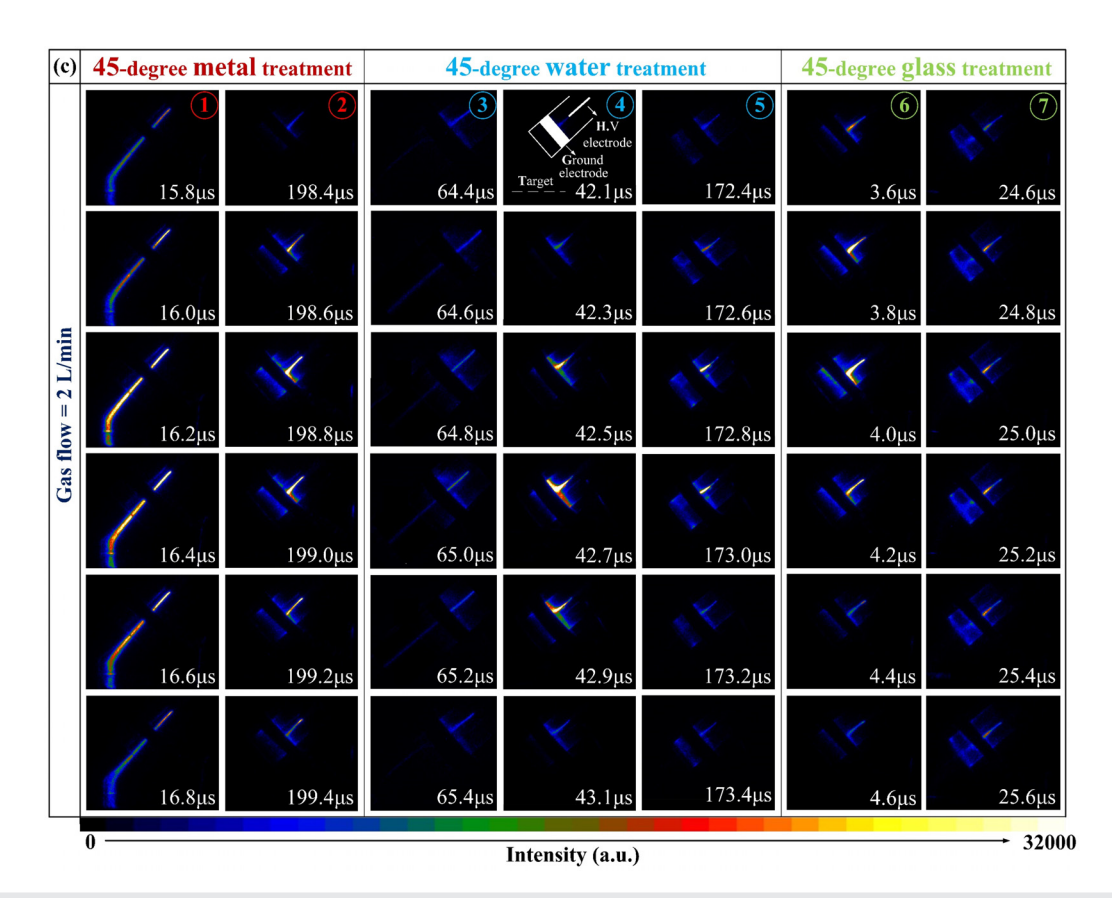


FIG. 6. Time-resolved images of the plasma jet at an incidence angle of 45° with metal, water, and glass treatment at gas flow rate of 2 L/min.

incidence angles. With the further increase in incidence angles from 45° to 60°, the emission intensity of water case at H-G region increases by 14.9%, at G-T region increases by 34.5%, while that of glass case at H-G region increases by 13.9%, at G-T region increases by 10.7%, respectively. Therefore, the incidence angle has much impact on the water case than the glass case, which indicates that the angle of the APPJ with respect to the surface could be used as a control mechanism to activate a liquid.¹⁷

D. Equivalent circuit

1. Equivalent circuit model

The equivalent circuit model was applied to analyze the electrical behavior of the plasma discharge, which is shown in Fig. 9. The capacitor C_d is the equivalent capacitance of the quartz tube while C_s denotes the stray capacitance between the H.V. electrode and the grounded electrode. The capacitors C_g and C_p stand for the equivalent capacitances of the discharge gap and the plasma plume in ambient air, respectively.

According to the dynamic images in Figs. 4–7, the equivalent model corresponds to both discharge regions: glow-like DBD and plasma jet interacting with substrates. As the applied voltage is enough to induce breakdown between the H.V. inner electrode and grounded outer electrode, the discharge mode could be characterized as a glow-

like DBD. In this scenario, the discharge region within the whole quartz tube stands for the discharge gap observed in a plane-plate DBD setup, which is similar to the DBD description in other works. 42,43 Therefore, the equivalent electric model representing the DBD plasma within the quartz tube could be illustrated as an RC circuit of variable value $R_{\rm g}(t)$ and $C_{\rm g}(t)$, as shown in Fig. 9(a). A voltage-controlled current source (VCCS) is employed to represent the discharge current of DBD in the gas gap, whose characteristic is determined by the applied voltage. From Figs. 3–7, the peak discharge current and its corresponding to the luminous intensity of plasma between the H.V. electrode and grounded electrode (DBD mode) show almost the same value, which is not related to the substrates treated by plasma jet.

Figure 9(b) shows the plasma transits from the grounded electrode and then extends beyond the quartz tube to generate a plasma jet that interacts with the substrates. Within the quartz tube, the discharge occurring in the inter-electrode gap between the H.V. electrode and grounded electrode remains a DBD mode, whose equivalent electrical circuit model is the same as that in Fig. 8(a). It should be noted that the C_g , the equivalent capacitance of gap capacity (i.e., the capacity of plasma in the gap), is determined by its charge q_g (concentrated mainly in the near-wall charge layers): $C_g = q_g/V_g$. However, the charge q_g is determined not by the applied voltage V_g at a given time, as in the case of a conventional capacitor, but by the state of the plasma in the gap,

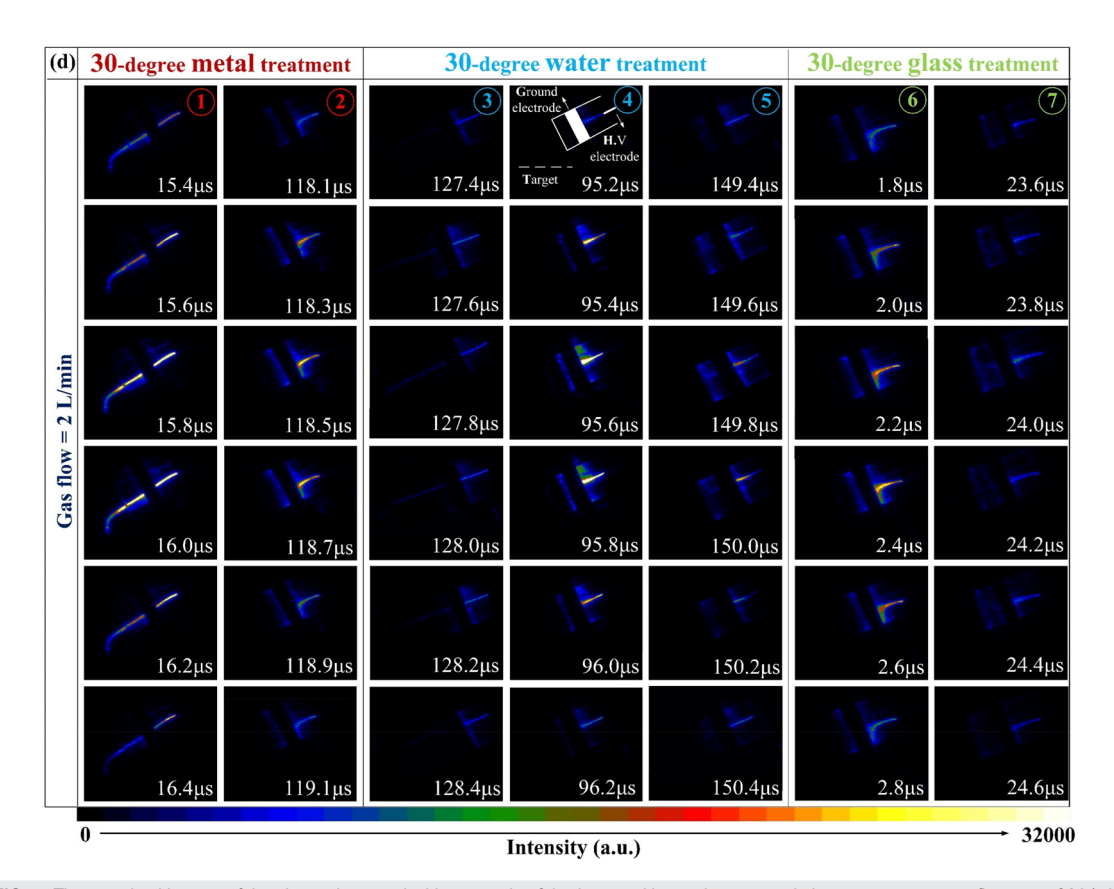


FIG. 7. Time-resolved images of the plasma jet at an incidence angle of 45-degree with metal, water, and glass treatment at gas flow rate of 2 L/min.

which is determined by some preceding time interval. Therefore, it cannot be assumed that $C_{\rm g}$ is a constant. The propagation of plasma jet in surrounding air outside the quartz tube modifies the value of relative permittivity of the air, therefore altering its equivalent resistance. Correspondingly, the electrical model of plasma plume in the quartz tube outlet can be defined by a variable capacitor $C_{\rm p}(t)$ in series with a variable resistance $R_{\rm p}(t)$. Since $C_{\rm p}(t)$ is determined by its charge

 $q_{\rm p}$ (the part of charge in plasma plume): $C_{\rm p}=q_{\rm p}/V_{\rm p}$, which is related to the length of the plasma plume in ambient air, it is also different from the case of a conventional capacitor. With the plume extending further in air with increasing applied voltage, $C_{\rm p}$ (t) decreases and $R_{\rm p}$ (t) increases. 43

When the plasma jet is used to treat three kinds of substrates, they can be integrated as parallel connection of resistance R (t) and

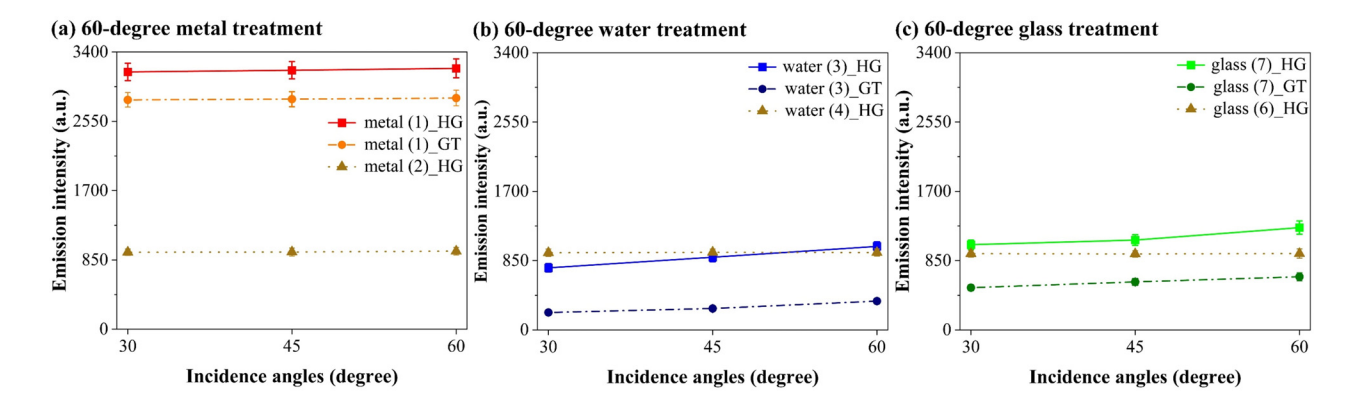


FIG. 8. Mean value of light intensity in one discharge cycle at various current pulses as a function of incidence angles. The abbreviations included in the FIG are as follows: HG (high-voltage electrode–ground electrode region) and GT (ground electrode–target region).

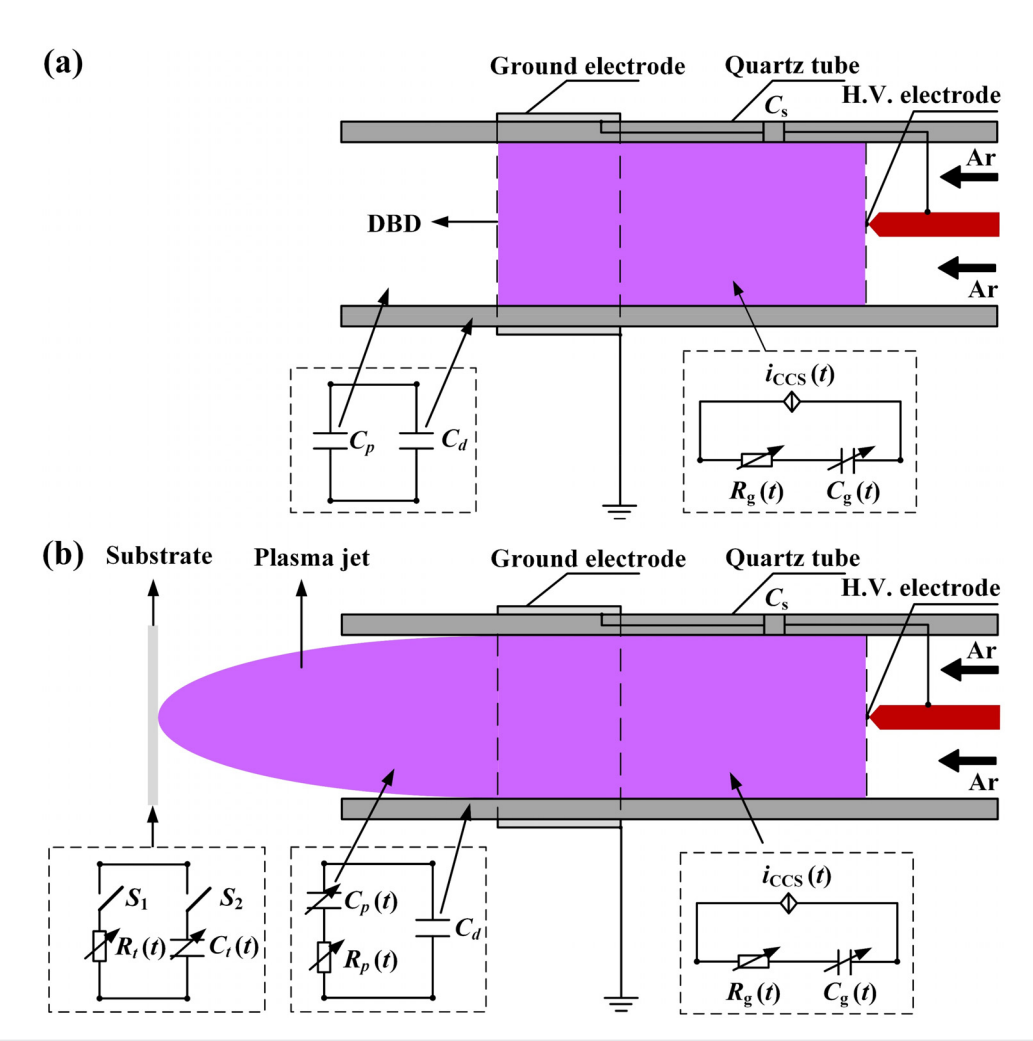


FIG. 9. Equivalent electrical models of the discharge (a) during DBD and (b) during jet discharge interact with substrates

capacitance C(t) with the assistance of switches indicating whether the branch is on or off. The metal substrates could be treated as a fixed resistance R with S_1 on and S_2 off (only resistor branch on). The glass plate could be treated as a fixed capacitance C with S_1 off and S_2 on (only capacitor branch on). For water treatment, it can be interpreted as the parallel connection of a variable capacitor $C_t(t)$ and a variable resistor $R_t(t)$ with both S_1 and S_2 on (both resistor and capacitor branches on).

2. Equivalent circuit diagrams

The equivalent electrical diagrams reveal the dynamic electrical behaviors of the plasma jet at two stages, i.e., DBD mode and plasma jet treatment mode, which are shown in Figs. 10(a) and 10(b), respectively. In Fig. 10, $R_{\rm e}$, $C_{\rm e}$, and $L_{\rm e}$ are represented as the inner impedance of excitation source and circuit wire. The applied voltage from the power source, voltage across the gas gap, voltage across dielectric barrier (quartz tube), and plasma jet voltage are simulated as $V_{\rm a}(t)$, $V_{\rm g}(t)$, $V_{\rm d}(t)$, and $V_{\rm t}(t)$ in the electric circuit model. The series of current

 $i_{\rm a}$ (t), $i_{\rm g}$ (t), $i_{\rm CCS}$ (t), and $i_{\rm S}$ (t) represent different parts of current as total external circuit current, discharge current in the gas gap, displacement current in the dielectric barrier (quartz tube), plasma jet current, and the displacement current through $C_{\rm S}$, respectively. According to Kirchhoff's theorem, the discharge characteristics can be calculated from Fig. 10(b), 31

$$i_a(t) = i_d(t) = C_d \frac{dV_d(t)}{dt},\tag{1}$$

$$i_g(t) = i_a(t) - i_{VCCS}(t) = C_g \frac{dV_g(t)}{dt} + V_g \frac{dC_g}{dt}, \qquad (2)$$

$$V_a(t) = V_g(t) + V_d(t). \tag{3}$$

From Eqs. (1)–(3), i_{VCCS} can be deduced as follows:

$$i_{VCCS}(t) = \left(1 + \frac{C_g}{C_d}\right)i_a(t) - C_g \frac{dV_g(t)}{dt} + V_g \frac{dC_g}{dt}.$$
 (4)

By integrating Eq. (1), the dielectric voltage $V_{\rm d}$ (t) is obtained as

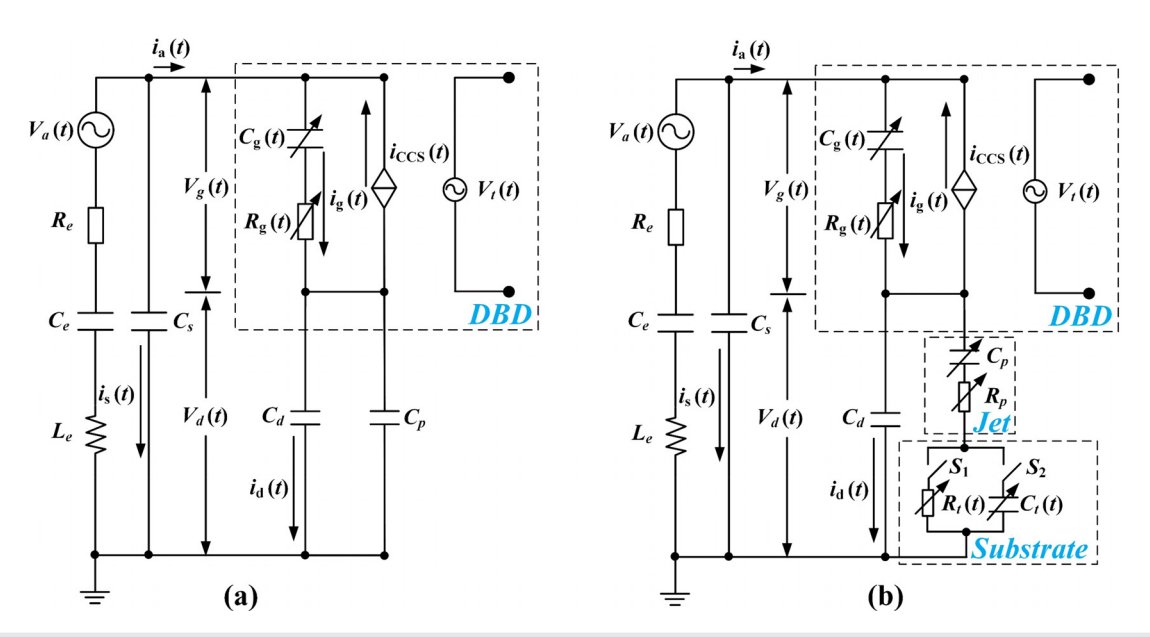


FIG. 10. Equivalent circuit diagrams of the discharge (a) during DBD, (b) during jet discharge with target.

$$V_{a}(t) = \frac{1}{C_{d}} \int_{0}^{t} i_{a}(\tau) d\tau + V_{g}(0).$$
 (5)

The gap voltage $V_{\rm g}$ can be obtained by substituting (5) into (3), thus giving

$$V_a(t) = V_a(t) - \frac{1}{C_d} \int_0^t i_a(\tau) d\tau - V_g(0).$$
 (6)

In Eqs. (5) and (6), $V_{\rm d}$ (0) corresponds to the memory voltage that is a consequence of the charge accumulated in the previous time interval, which is related to the applied voltage $V_{\rm a}$ (t). In Eqs. (4) and (6), $i_{\rm VCCS}$ is not only governed by the external measurable parameters $i_{\rm a}$ (t) and $V_{\rm a}$ (t) but also related to the time-resolved capacitor $C_{\rm g}$ (t).

Considering the plasma jet with different incidence angles impinging on metal, water, and glass substrates, decreasing the incidence angle between jet and target generally results in a wider surface area covered by the plasma, thus accordingly changing the composition of equivalent resistor and capacitor in the circuit. For metal treatment, although the surface area was increased when the incidence angle was decreased from 60° to 30°, the equivalent resistor will not change due to the conductive characteristic of metal plate. Therefore, the peak discharge current and its corresponding to the luminous intensity of plasma would remain the same conditions. For glass treatment, a wider surface area will increase the value equivalent capacitor $C_t(t)$, thus increasing the impedance of the circuit. Therefore, the peak discharge current and its corresponding to the luminous intensity of plasma would decrease, which are in line with the results of the discharge currents and dynamic process. For the water treatment, the parallel connection of a capacity C_t (t) and a resistance R_t (t) will change with the treatment time, which accounts for the random discharge during the period. With the increase in treatment time, $C_t(t)$ decreases and $R_t(t)$ increases, so the peak discharge current and its corresponding to the luminous intensity of plasma would decrease.4

3. Model comparison with other works

Figure 11 shows another approach for the equivalent electrical circuits of the "plasma jet—substrate" system is to separate between the "core," the "effluent" plasma and the "substrate," which is offered in the literature. ^{29,30} The "core" can be interpreted as a DBD ignited between the high-voltage electrode and the grounded electrode. After the core ignition, a second discharge channel is formed, generating the visible plasma referred to as the "effluent," which then impacts the substrate plate at a floating potential. ⁴⁸ Each discharge can be represented by the series connection of a resistance (R_1 , R_2) and a capacity (C_1 , C_2). $C_{\rm air}$ suggests that the "effluent" is coupled via the ambient air toward any mass close by, which is challenging to determine. The three kinds of substrates can be integrated as parallel connection of resistor and capacitor C with the assistance of switches, which is the same as that in Fig. 10.

It is important to note that both the equivalent circuits could give a general insight into the plasma source based on different emphasis. In general, DBD is characterized by large number of filaments (termed micro-discharges). The electrical equivalence models in Fig. 10 mainly focus on the simulation of the micro-discharges in the gas gap, represented by a CCS, an equivalent resistance $R_{\rm g}$ (t), and a non-linear variable capacitance $C_{\rm g}$ (t). The model with a CCS follows the multitude and attenuation of the micro-discharges according to the slope of the applied voltage, and it can present the dynamic state in the gap. On the other hand, the electrical equivalence model in Fig. 11 is more simplified than that in Fig. 10, which is based on the geometry of the "plasma jet—substrate" system by separating between three electrodes, i.e., the "core," the "effluent" plasma and the "substrate." With a surface as a third electrode, the impact on the electrical circuit starts to act only after a certain voltage is reached to bridge the additional gap [e.g., $C_t(t)$].

The equivalent electrical models depicted in Figs. 10 and 11 are generic, flexible, and easy-to-implement tools as they could effectively analyze the electrical characteristic such as current and power to

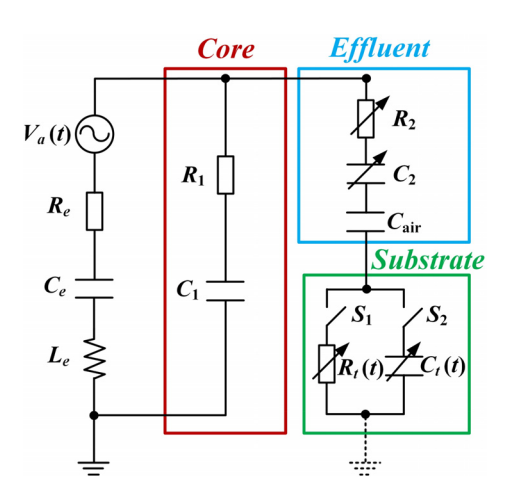


FIG. 11. Another electrical equivalence circuit for the discharge at the "core," the "effluent" and the "substrate." R_1 and R_2 represent the effective resistances of DBD plasma and plasma jet; and C_1 and C_2 represent the capacitance of DBD plasma and plasma jet. $C_{\rm alir}$ is the capacitance of the surrounding air.

investigate the distribution of the energy deposition into DBD plasma region and in plasma jet itself. The values of $C_{\rm S}$ can be measured with plasma off operation. To characterize the specific results of the varying plasma impedance at different discharge stages, the values of other important electric components $[C_{\rm g}(t),\,R_{\rm g}(t),\,C_{\rm p}(t),\,$ and $R_{\rm p}(t)]$ can be defined by solving fluid balance equations for all species of charged and neutral particles and the electron temperature, supplemented by the Poisson equation for finding a self-consistent electric field, which could be further investigated.

However, these equivalent electrical models could not predict the non-linear behavior in plasma due to complex interactions between charged particles, neutral particles, and electromagnetic fields; spatial variations on properties such as electron density, temperature, and electric field as equivalent circuit models usually represent averaged properties; particle interactions like plasma-generated reactive species transported to the substrate often simplified or not included in equivalent circuits. In addition, higher energy deposition in plasma jet would benefit a good repetition of DBD working regime from one period to another. To perform plasma-generated reactive species research, it is better to work at higher velocity that could avoid fast mixing of the blowing out argon flow with the electronegative ambient air.

IV. CONCLUSION

The effect of non-perpendicular incidence angles (60°, 45°, and 30°) and gas flow rate on discharge behavior and discharge current of an AC argon plasma jet interacting with an ungrounded metal, water, and glass plate was investigated. The peak value of discharge current at only the H-G region (DBD stage) was almost the same 20 mA. The mean luminous intensity at the G-T region for water and glass surfaces decreased by 39.5% and 20.5% when the incidence angle decreased from 60° to 30°, respectively. However, the incidence angle and the gas flow rate had no significant difference in discharge characteristics of plasma jet for the metal case. The equivalent circuit analysis shows two discharge regions: glow-like DBD and jet interacting with substrates, representing parallel connection of resistance and capacitance with switches on/off. Thus, the decrease in incidence angle has a

negative impact on the titled plasma jet for water and glass treatment due to the modification of equivalent impedance.

ACKNOWLEDGMENTS

Jiayin Li and Minkwan Kim acknowledge funding from U.K. Space Agency, "All-in-One Mars *In situ* Resource Utilisation System using Non-thermal Plasma" (Grant No. UKSAG22_ESE01) and European Space Agency, "Plasma Air Sterilisation and Treatment Apparatus (PASTA) (Grant No. 4000140067/22/NL/AL/mma).

AUTHOR DECLARATIONS Conflict of Interest

The authors have no conflicts to disclose.

Author Contributions

Jiayin Li: Conceptualization (equal); Data curation (equal); Writing – original draft (equal). **Minkwan Kim:** Resources (equal); Supervision (equal); Writing – review & editing (equal).

DATA AVAILABILITY

The data that support the findings of this study are available from the corresponding author upon reasonable request.

REFERENCES

- ¹T. Shao, Y. Zhou, C. Zhang, W. Yang, Z. Niu, and C. Ren, "Surface modification of polymethyl-methacrylate using atmospheric pressure argon plasma jets to improve surface flashover performance in vacuum," IEEE Trans. Dielect. Electr. Insul. 22(3), 1747–1754 (2015).
- ²V. Prysiazhnyi, V. F. B. Saturnino, and K. G. Kostov, "Transferred plasma jet as a tool to improve the wettability of inner surfaces of polymer tubes," Int. J. Polym. Anal. Ch. 22(3), 215–221 (2017).
- ³D. Shaw, A. West, J. Bredin, and E. Wagenaars, "Mechanisms behind surface modification of polypropylene film using an atmospheric-pressure plasma jet," Plasma Sources Sci. Technol. 25(6), 065018 (2016).
- ⁴K. G. Kostov, T. M. C. Nishime, A. H. R. Castro, A. Toth, and L. R. O. Hein, "Surface modification of polymeric materials by cold atmospheric plasma jet," Appl. Surf. Sci. 314, 367–375 (2014).
- ⁵A. Lin, M. Gromov, A. Nikiforov, E. Smits, and A. Bogaerts, "Characterization of non-thermal dielectric barrier discharges for plasma medicine: From plastic well plates to skin surfaces," Plasma Chem. Plasma Process. 43(6), 1587–1612 (2023).
- ⁶M. G. Kong, G. Kroesen, G. Morfill, T. Nosenko, T. Shimizu, J. van Dijk, and J. L. Zimmermann, "Plasma medicine: An introductory review," New J. Phys. 11(11), 115012 (2009).
- ⁷H. Xu, D. Liu, W. Wang, Z. Liu, L. Guo, M. Rong, and M. G. Kong, "Investigation on the RONS and bactericidal effects induced by He + O₂ cold plasma jets: In open air and in an airtight chamber," Phys. Plasmas 25(11), 113506 (2018).
- ⁸J. Lin, J. Zhang, R. Zhou, L. Guo, D. Liu, M. Rong, M. G. Kong, and K. Ostrikov, "Plasma-enhanced microbial electrolytic disinfection: Decoupling electro- and plasma-chemistry in plasma-electrolyzed oxidizing water using ion-exchange membranes," Water Res. 225, 119174 (2022).
- ⁹G. R. Stratton, C. L. Bellona, F. Dai, T. M. Holsen, and S. M. Thagard, "Plasmabased water treatment: Conception and application of a new general principle for reactor design," Chem. Eng. J. 273, 543–550 (2015).
- ¹⁰Q. Yang, J.-J. Qiao, H. Cheng, and Q. Xiong, "Plasma-liquid interactions: An experiment and simulation study on plasma dynamic behaviors near the gas-liquid interfacial layer," Plasma Sources Sci. Technol. 32(9), 095013 (2023).

- ¹¹K. Hadinoto, N. R. H. Rao, J. B. Astorga, R. Zhou, J. Biazik, T. Zhang, H. Masood, P. J. Cullen, S. Prescott, R. K. Henderson, and F. J. Trujillo, "Hybrid plasma discharges for energy-efficient production of plasma-activated water," Chem. Eng. J. 451, 138643 (2023).
- ¹²O. V. Penkov, M. Khadem, W.-S. Lim, and D.-E. Kim, "A review of recent applications of atmospheric pressure plasma jets for materials processing," J. Coat. Technol. Res. 12(2), 225–235 (2015).
- ¹³X. Lu, D. Liu, Y. Xian, L. Nie, Y. Cao, and G. He, "Cold atmospheric-pressure air plasma jet: Physics and opportunities," Phys. Plasmas 28(10), 100501 (2021).
- ¹⁴S. Bornholdt, M. Wolter, and H. Kersten, "Characterization of an atmospheric pressure plasma jet for surface modification and thin film deposition," Eur. Phys. J. D 60(3), 653–660 (2010).
- ¹⁵K. Urabe, T. Morita, K. Tachibana, and B. N. Ganguly, "Investigation of discharge mechanisms in helium plasma jet at atmospheric pressure by laser spectroscopic measurements," J. Phys. D: Appl. Phys. 43(9), 095201 (2010).
- ¹⁶L. Wang, Y. Zheng, and S. Jia, "Numerical study of the interaction of a helium atmospheric pressure plasma jet with a dielectric material," Phys. Plasmas 23(10), 103504 (2016).
- ¹⁷G. Parsey, A. M. Lietz, and M. J. Kushner, "Guided plasma jets directed onto wet surfaces: Angular dependence and control," J. Phys. D: Appl. Phys. 54(4), 045206 (2020).
- ¹⁸T. M. C. Nishime, R. Wagner, and K. G. Kostov, "Study of modified area of polymer samples exposed to a He atmospheric pressure plasma jet using different treatment conditions," Polymers 12(5), 1028 (2020).
- ¹⁹X. Damany, S. Pasquiers, N. Blin-Simiand, G. Bauville, B. Bournonville, M. Fleury, P. Jeanney, and J. S. Sousa, "Impact of an atmospheric argon plasma jet on a dielectric surface and desorption of organic molecules," Eur. Phys. J. Appl. Phys. 75(2), 24713 (2016).
- ²⁰M. Hosseinpour, A. Zendehnam, S. M. Hamidi Sangdehi, and H. Ghomi Marzdashti, "Effects of different gas flow rates and non-perpendicular incidence angles of argon cold atmospheric-pressure plasma jet on silver thin film treatment," J. Theor. Appl. Phys. 13(4), 329–349 (2019).
- ²¹E. Slikboer, A. Sobota, O. Guaitella, and E. Garcia-Caurel, "Imaging axial and radial electric field components in dielectric targets under plasma exposure," J. Phys. D: Appl. Phys. 51(11), 115203 (2018).
- ²²S. Razavizadeh, H. Ghomi, and A. Sobota, "Atmospheric pressure plasma jet in controlled atmosphere: Electric fields and propagation dynamics," Plasma Sources Sci. Technol. 27(7), 075016 (2018).
- ²³G. Liu, Y. Xia, L. Han, K. Shang, and D. Liu, "Interaction of atmospheric pressure helium plasma jet with tilted dielectric target: Split and deviation of ionization waves," J. Phys. D: Appl. Phys. 56(17), 175203 (2023).
- ²⁴N. Y. Babaeva, G. V. Naidis, D. V. Tereshonok, C. Zhang, B. Huang, and T. Shao, "Interaction of helium plasma jet with tilted targets: Consequences of target permittivity, conductivity and incidence angle," Plasma Sources Sci. Technol. 30(11), 115021 (2021).
- ²⁵W.-K. Chen, J.-C. Huang, Y.-C. Chen, M.-T. Lee, and J.-Y. Juang, "Deposition of highly transparent and conductive Ga-doped zinc oxide films on tilted substrates by atmospheric pressure plasma jet," J. Alloy. Compd. 802, 458–466 (2019).
- ²⁶O. T. Olabanji and J. W. Bradley, "Side-on surface modification of polystyrene with an atmospheric pressure microplasma jet," Plasma Processes Polym. 9(9), 929–936 (2012).
- ²⁷B. L. M. Klarenaar, O. Guaitella, R. Engeln, and A. Sobota, "How dielectric, metallic and liquid targets influence the evolution of electron properties in a pulsed He jet measured by Thomson and Raman scattering," Plasma Sources Sci. Technol. 27(8), 085004 (2018).
- ²⁸ A. Sobota, O. Guaitella, G. B. Sretenović, V. V. Kovačević, E. Slikboer, I. B. Krstić, B. M. Obradović, and M. M. Kuraica, "Plasma-surface interaction: Dielectric and metallic targets and their influence on the electric field profile in a kHz AC-driven He plasma jet," Plasma Sources Sci. Technol. 28(4), 045003 (2019).
- ²⁹Y. S. Akishev, V. B. Karalnik, M. A. Medvedev, A. V. Petryakov, N. I. Trushkin, and A. G. Shafikov, "Influence of DC and AC external electric field on the

- propagation of 'plasma bullets' along DBD helium plasma jet," J. Phys.: Conf. Ser. 927(1), 012051 (2017).
- 30Y. S. Akishev, V. B. Karalnik, M. A. Medvedev, A. V. Petryakov, N. I. Trushkin, and A. G. Shafikov, "How ionization waves (plasma bullets) in helium plasma jet interact with a dielectric and metallic substrate," J. Phys.: Conf. Ser. 927, 012040 (2017).
- ³¹C. Zhang, T. Shao, Y. Yu, Z. Niu, P. Yan, and Y. Zhou, "Comparison of experiment and simulation on dielectric barrier discharge driven by 50 Hz AC power in atmospheric air," J. Electrostat. 68(5), 445–452 (2010).
- ³²P. Viegas, E. Slikboer, Z. Bonaventura, O. Guaitella, A. Sobota, and A. Bourdon, "Physics of plasma jets and interaction with surfaces: Review on modelling and experiments," Plasma Sources Sci. Technol. 31(5), 053001 (2022).
- ³³R. Bussiahn, E. Kindel, H. Lange, and K.-D. Weltmann, "Spatially and temporally resolved measurements of argon metastable atoms in the effluent of a cold atmospheric pressure plasma jet," J. Phys. D: Appl. Phys. 43(16), 165201 (2010).
- ³⁴R. Wang, H. Xu, Y. Zhao, W. Zhu, K. Ostrikov, and T. Shao, "Effect of dielectric and conductive targets on plasma jet behaviour and thin film properties," __J. Phys. D: Appl. Phys. 52(7), 074002 (2018).
- 35S. A. Norberg, E. Johnsen, and M. J. Kushner, "Helium atmospheric pressure plasma jets interacting with wet cells: Delivery of electric fields," J. Phys. D: Appl. Phys. 49(18), 185201 (2016).
- ³⁶I. Jögi, R. Talviste, S. Raud, J. Raud, T. Plank, L. Moravský, M. Klas, and Š. Matejčík, "Comparison of two cold atmospheric pressure plasma jet configurations in argon," Contrib. Plasm. Phys. 60(3), e201900127 (2020).
- ³⁷Y. Akishev, G. Aponin, A. Balakirev, M. Grushin, V. Karalnik, A. Petryakov, and N. Trushkin, "DBD surface streamer expansion described using nonlinear diffusion of the electric potential over the barrier," J. Phys. D: Appl. Phys. 46(46), 464014 (2013).
- ³⁸O. Guaitella and A. Sobota, "The impingement of a kHz helium atmospheric pressure plasma jet on a dielectric surface," J. Phys. D: Appl. Phys. 48(25), 255202 (2015).
- 39A. Sarani, A. Yu. Nikiforov, and C. Leys, "Atmospheric pressure plasma jet in Ar and Ar/H₂O mixtures: Optical emission spectroscopy and temperature measurements," Phys. Plasmas 17(6), 063504 (2010).
- ⁴⁰B. Huang, C. Zhang, W. Zhu, X. Lu, and T. Shao, "Ionization waves in nanosecond pulsed atmospheric pressure plasma jets in argon," High Voltage 6(4), 665–673 (2021).
- ⁴¹R. Wang, H. Sun, W. Zhu, C. Zhang, S. Zhang, and T. Shao, "Uniformity optimization and dynamic studies of plasma jet array interaction in argon," Phys. Plasmas 24(9), 093507 (2017).
- ⁴²D. Zhou, Q. Liu, H. Zhang, J. Li, L. Zhou, and T. Zhang, "Investigation of the behavior of plasma jet in the presence of water under different grounded conditions." Contrib. Plasm. Phys. 64(3), e202300080 (2024).
- ⁴³Z. Fang, T. Shao, J. Yang, and C. Zhang, "Discharge processes and an electrical model of atmospheric pressure plasma jets in argon," Eur. Phys. J. D 70(1), 3 (2016).
- 44Z. Fang, S. Ji, J. Pan, T. Shao, and C. Zhang, "Electrical model and experimental analysis of the atmospheric-pressure homogeneous dielectric barrier discharge in He," IEEE Trans. Plasma Sci. 40(3), 883–891 (2012).
- ⁴⁵U. N. Pal, P. Gulati, N. Kumar, R. Prakash, and V. Srivastava, "Multiswitch equivalent electrical model to characterize coaxial DBD tube," IEEE Trans. Plasma Sci. 40(5), 1356–1361 (2012).
- 46N. Y. Babaeva, G. V. Naidis, V. A. Panov, R. Wang, S. Zhang, C. Zhang, and T. Shao, "Plasma bullet propagation and reflection from metallic and dielectric targets," Plasma Sources Sci. Technol. 28(9), 095006 (2019).
- ⁴⁷J. Lin, D. Liu, J. Zhang, R. Zhou, M. Rong, and K. Ostrikov, "Insights into reactivity and bactericidal effects of water activated by He and Ar plasma jets," Plasma Processes Polym. 20(4), 2200173 (2023).
- ⁴⁸T. Gerling, R. Brandenburg, C. Wilke, and K.-D. Weltmann, "Power measurement for an atmospheric pressure plasma jet at different frequencies: Distribution in the core plasma and the effluent," Eur. Phys. J. Appl. Phys. 78(1), 10801 (2017).